

Open-path cavity ring-down methane sensor for mobile monitoring of natural gas emissions

Laura E. Mchale,¹ Benjamin Martinez,¹ Thomas W. Miller,² and Azer P. Yalin^{1,*}

¹Department of Mechanical Engineering, Colorado State University, Fort Collins, CO 80525, USA

²TCB Engineers, Surprise, AZ 85374, USA

*azer.yalin@colostate.edu

Abstract: We present the design, development, and testing results of a novel laser-based cavity ring-down spectroscopy (CRDS) sensor for methane detection. The sensor is specifically oriented for mobile (i.e. vehicle deployed) monitoring of natural gas emissions from oil and infrastructure. In contrast to most commercial CRDS sensors, we employ an open-path design which allows higher temporal response and a lower power and mass package more suited to vehicle integration. The system operates in the near-infrared (NIR) at 1651 nm with primarily telecom components and includes cellular communication for wireless data transfer. Along with basic sensor design and lab testing, we present results of field measurements showing performance over a range of ambient conditions and examples of methane plume detection.

© 2019 Optical Society of America under the terms of the [OSA Open Access Publishing Agreement](#)

1. Introduction

Methane is widely viewed as a “bridge fuel” that can backfill energy needs as we transition to renewable energy sources such as solar and wind. It is touted as a “clean fuel” given that it produces less carbon dioxide (CO₂) than coal or gasoline during combustion; however, it is important that it is a significant greenhouse gas in its own right. The latest report from the Intergovernmental Panel on Climate Change (IPCC) lists its 20 year Global Warming Potential (GWP₂₀) as 84 times that of CO₂ [1]. Methane is also a precursor to tropospheric ozone formation through reactions of methane and the hydroxyl radical, which also diminishes the oxidizing abilities of the atmosphere through removal of hydroxyl radical.

Natural gas (which is generally ~80-95% methane) has seen a recent rise in use and extraction, contributing to the increase in atmospheric methane concentrations [2]. For example, the Colorado Oil and Gas conservation Commission (COGCC) estimates that there are more than 40,000 active wells in the state, with more than 10,000 new wells since 2005 [3]. The natural gas supply chain consists of a series of segments generally referred to as extraction, gathering and processing, transmission, storage and distribution. Given the high GWP₂₀ value of methane, it is clearly critical to minimize any emissions (planned or fugitive) along this supply chain prior to final use in combustion systems [4].

To quantify, locate and reduce methane emissions, there is a need for quantitative measurement tools over a range of spatial scales. At larger spatial scales (order kms), for example to cover entire “basins”, airplane mounted sensors can be used with mass balance approaches to estimate emissions [5–7]. A number of ongoing and new efforts are also developing satellite systems for emissions measurements (e.g., [8–10]). The spatial resolution (granularity) afforded by satellite measurements will vary between systems but is generally on the km scale [11,12].

Our interest is to develop measurement tools that can be used on the scale of individual well sites (order 10 m spatial resolution) to allow quantification of emissions, preferably in a

scalable (“high-throughput”) manner to measure many potential emission sites (e.g. wells) per unit time. Such measurement capability would be useful for industry to monitor their sites (and identify and repair anomalies), as well as for researchers and regulators, for example to reconcile “bottom-up” (component level) versus “top-down” (aircraft) measurements [13,14]. Currently, the industry standard is to have personnel perform manual inspections with optical gas imaging (OGI) cameras [15]; these measurements are usually only qualitative. Examples of other instruments used by industry include a vehicle-mounted laser absorption sensor (with sensitivity of ~ 1 ppm) [16], and a hand-held laser absorption based detector used to detect leaks by on-site personnel [17].

An approach that may be scalable to efficiently cover many sites is mobile sensing, i.e., deploying sensors on vehicles (generally automobiles, but also unmanned aerial vehicles) and then combining the sensor CH_4 concentration values with the local wind field to locate and quantify emission sources [18–20]. In principle, such measurements can be performed with a range of sensors as long as they yield sufficient sensitivity, time response, and accuracy to faithfully capture the methane plumes (amplitude and position), i.e. elevated readings above ambient background due to emission sources [21–23]. Recent data from the United States Environmental Protection Agency [24] indicate that a sensitivity of ~ 100 ppb is very adequate for practical emissions monitoring and leak detection (see also concluding discussion in Section 5). The needed time response (and measurement rate) for vehicle sampling is ~ 1 s as this corresponds to distances of ~ 10 -30 m for drive speeds (of ~ 30 -100 km/hr) allowing relatively accurate plume locating. Poorer time resolution and/or lag time (from flow cells) can distort mobile data and complicate the proper locating of readings [25,26] and [27] (see also supplemental material). Insufficient accuracy in concentrations will translate to error in mass flow inference (also limited by variations from turbulent transport), but ~ 3 -10% may be sufficient for practical cases. Practical deployment on mobile platforms also requires adequate SWAP (i.e. size, weight, and packaging) as is discussed herein.

Here, we report on a purpose built sensor for mobile methane sampling. The sensor is based on the cavity ring-down spectroscopy (CRDS) technique [28,29] allowing sensitive (and specific) methane detection. We use an open-path configuration, where air that flows through the open-cavity (on the vehicle roof) is directly sampled, which allows for high time response, relatively low-power (< 30 W without heaters; < 150 W with heaters) and compact designs amenable to vehicle integration. (This is in contrast to commonly used closed-path CRDS sensors, with pumps, that can have poor time response and typically consume ~ 300 -500 W of power and have mass of ~ 30 -50 kg.) Open-path operation leads to measurement “noise” from particles in the air and our past work has shown the use of software filtering to mitigate those effects [30]. In Section 2 of this contribution, we detail the spectroscopic underpinning and optical design of the sensor as well as sensor packaging and vehicle integration. Section 3 describes laboratory testing of accuracy and sensitivity, while Section 4 describes field testing of the sensor examining performance across ambient conditions (e.g. as temperature and vehicle speed vary) as well as examples of plume detection from oil and gas equipment. Finally, conclusions and directions for future are presented in Section 5.

2. Sensor design

2.1. Overview: open-path cavity ring-down sensor

CRDS is a direct absorption measurement technique in which an absorbing sample is housed within a high-finesse optical cavity typically formed from a pair of high-reflectivity (HR) mirrors [28,29]. The rate of light decay inside the cavity, i.e. the ring-down time, is recorded from which the sample concentration can be determined through the Beer-Lambert law. CRDS offers high sensitivity as well as high specificity to the target analyte. A distinguishing feature of our sensor is the simple “open-path” configuration where the ambient air is directly sampled between the mirrors with no inlet or flow cell [30]. This is in contrast to most CRDS sensors – or other sensors using related techniques - employing “closed-path” configurations

where a vacuum pump pulls the sample through an inlet and flow cell located between HR mirrors [31–33]. An immediate advantage of open-path for mobile sampling is the improved time response (essentially instantaneous relative to flow time-scales) meaning that the spatial shapes of observed plumes are faithfully recorded, while other benefits are associated with ease of vehicle integration, i.e. reduced power draw and sensor mass as discussed in Section 3. When closed-path flow systems are used, there is a time lag associated with passage of the sampled gas through the inlet to the cavity as well as potential broadening of impulsive signals. For example, past work by Von Fischer and colleagues with closed-path CRDS has found varying lags of ~3-9 s (corresponding to spatial shifts of ~50-150 m for typical vehicle speeds) which complicate analysis [34,35]. More generally, several studies have recognized the deleterious effects of insufficient time response to mobile sampling applications [25,26].

The closed-path flow cell architecture is primarily used to lower the sample pressure, typically to ~0.1 atm, to narrow the spectral lines as well as fix pressure and temperature which are necessary to determine gas concentration. The inlet also allows use of an inline particle filter for the dual purpose of 1) maintaining HR mirror reflectivity while also 2) reducing signal fluctuations due to additional (varying) optical loss from Mie scattering by particles in the beam path [36]. Our past work has shown that with appropriate software filters (against the Mie scatter noise) one can still maintain very adequate sensitivity [30]. Here, we focus on the design and field testing of an open-path methane CRDS sensor with emphasis on field performance in real outdoor ambient conditions.

2.2. Spectral simulations

In CRDS, the analyte species concentration is found by recording the ring-down times, $\tau(\nu)$, versus laser frequency, which can be readily converted to absorption coefficients $k(\nu)$. Figure 1 shows a simulated absorption spectrum (given as vacuum wavelength) for the conditions of interest including 4 methane absorption lines (6057.08, 6057.13, 6057.09, and 6057.10 cm^{-1} ; which blend into a single feature at ambient conditions) as well as proximate water and carbon dioxide absorption lines. The final spectrum is computed as the sum of the contributing features:

$$k(\nu) = b + \sum \phi_L(\nu, \nu_{0i}, \Delta\nu_i) P S_i n_i \quad (1)$$

where b is the cavity baseline loss (units of cm^{-1}), i is an index to sum over the needed lines, ϕ_L are frequency-normalized Lorentzian lineshapes (units of cm^{-1}) with center frequency ν_{0i} and width $\Delta\nu_i$ (units of cm^{-1}), P is the total pressure (units of atm), S_i the line strength (expressed in units of $\text{cm}^{-2}\text{atm}^{-1}$), and n_i the species concentration (in units of mole fraction). The use of Lorentzian lineshapes is justified by simulations showing that the effect of Doppler (thermal) broadening is negligible at atmospheric pressure. The spectroscopic constants ν_{0i} (given above), $\Delta\nu_i$ and S_i are from HITRAN 2012, where the width is found from the pressure broadening coefficient [37]. Equation (1) is used to simulate spectra as well as to fit CRDS measurements to retrieve concentrations. In the latter case, we employ 3 free fit-parameters: the baseline loss (from mirrors, diffraction, Rayleigh scattering and any possible broad spectrum absorption interferences), laser frequency offset (as the experiment uses relative frequency given slight drift in absolute laser frequency), and CH_4 concentration. (Note that while Fig. 1 includes the H_2O and CO_2 for purposes of exposition, we have also shown through simulation, that for the selected laser scan range, these non-methane species can be neglected from the spectral fits without compromising the retrieval accuracy of methane.) Accurate fitting requires knowledge of temperature and pressure which is achieved using real-time measurements of these parameters. Note that for plume detection, as opposed to long term ambient monitoring, one does not need to correct for dry air molar fractions since the water content (humidity) is relatively constant over the plumes (~10-100 m and ~10

s maximum); further, for inferring source mass-flow and location, the sensor directly measures methane number density (from which mole fraction can then be determined).

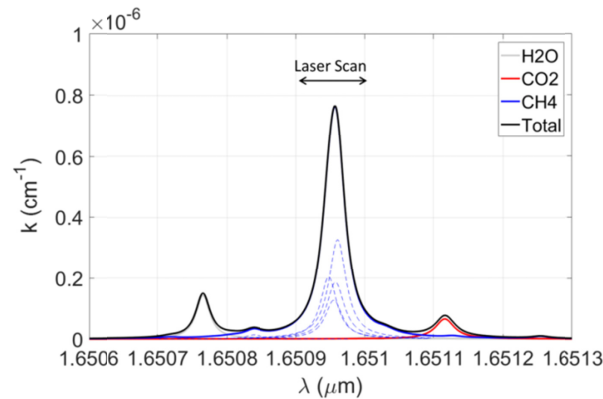


Fig. 1. Simulated open-path absorption spectrum for typical Colorado ambient conditions: $T = 296$ K, $P = 0.84$ atm, $[CH_4] = 1.8$ ppm, $[H_2O] = 50\%$ Relative Humidity, $[CO_2] = 380$ ppm. Dashed lines show the contributing CH_4 peaks.

2.3. Sensor opto-electronics

A schematic of the main opto-electronic aspects of the sensor is shown in Fig. 2. Most components are telecom based and therefore maturely engineered in terms of reliability, compactness and performance. The CRDS laser source is a continuous-wave distributed feedback (DFB) diode laser (NEL / NTT) in a 14-pin butterfly package operating in the vicinity of 1651 nm. The laser temperature is controlled by a thermo-electric cooler (TEC) mounted to the diode which fixes the overall wavelength region, and the spectrum is recorded by current-scanning of the laser. Compact (OEM-type) controllers are used for laser current and temperature control. Downstream, there is an inline fiber isolator (to prevent back reflections from the cavity to the laser) and a fiber coupled acousto-optic modulator which is used as an optical switch to quickly deflect the laser away from the cavity (to yield ring-down events). The laser output power is approximately 10 mW which, when measured after the isolator and AOM, becomes approximately 5 mW. Light exiting the final fiber after the AOM is passed to free-space via an adjustable focus aspheric FC collimator (Thorlabs CFC-8X-C). This lens is adjusted to achieve an approximately collimated beam spatially mode-matched to the optical cavity [38].

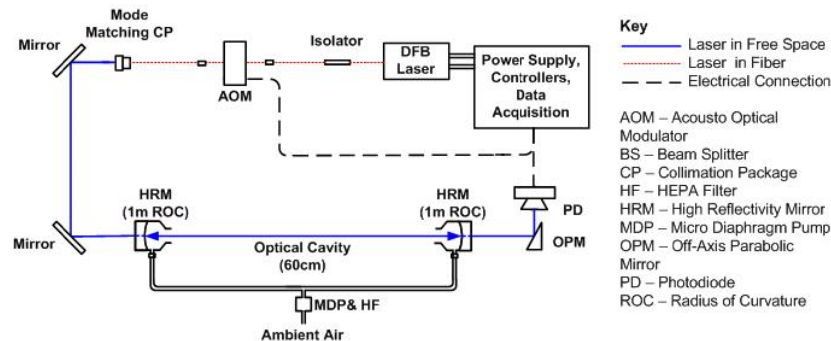


Fig. 2. Schematic diagram of CRDS methane sensor.

Two intermediate steering mirrors are used to inject the mode-matched beam to the dual-mirror optical cavity. The cavity is defined by two high-reflectivity (HR) mirrors separated by 60 cm. The HR mirrors (Advanced Thin Films) employ dielectric coatings on fused silica

substrates and have reflectivity of $R \sim 0.99994$ at 1651 nm. Light exiting the cavity is coupled with an off-axis parabolic mirror to a high-gain low-noise InGaAs photodetector amplifier module. The basic operational sequence is to scan the laser across the range of interest (Fig. 1) and, at each passage across a cavity resonance (where power is injected to the cavity and recorded with the exit detector), use a trigger circuit to turn off the AOM voltage (deflecting the beam away from the cavity) allowing a ring-down event to occur. A National Instruments sbRIO-9651 based on the Xilinx Zynq-7020 system on chip (SoC) is coupled with a custom carrier board to form the electronics platform core. Acquisition, triggering and laser scanning are implemented on the FPGA side of the SoC and ring-down fitting and analysis reside on the dual-core ARM Cortex-A9 CPU running a real-time operating system. The overall scan and trigger scheme follows past work from Lehmann's group [39] with more specific detail in our past publication [30].

2.4. Sensor packaging and vehicle integration

Figure 3 shows a solid model of the full sensor package. The sensor is comprised of two main assemblies: an optical head which contains the optical cavity (and detector) and an electronics enclosure which contains the microprocessor, controllers, circuitry and wireless gateway. The entire system was designed to handle a range of ambient conditions (temperature, vibration, possible precipitation and splash) while also optimizing size, weight and power (SWaP) for seamless vehicle integration. (An exception, as discussed below, is the enclosure used for the electronics box which, in this design iteration, was not yet optimized for size and weight.) The sensor is powered via direct connection (including inline fuse) to the vehicle battery ($\sim 12-18$ V). Given the open-path design (lack of main flow pump), the power draw is quite low - ranging between <30 W with heaters off to maximum of 150 W with heaters on - and does not affect the battery and vehicle operation. The sensor mounts to the vehicle via a standard roof-rack with a custom aluminum mount using wire-rope isolators to reduce the effects of vibration.

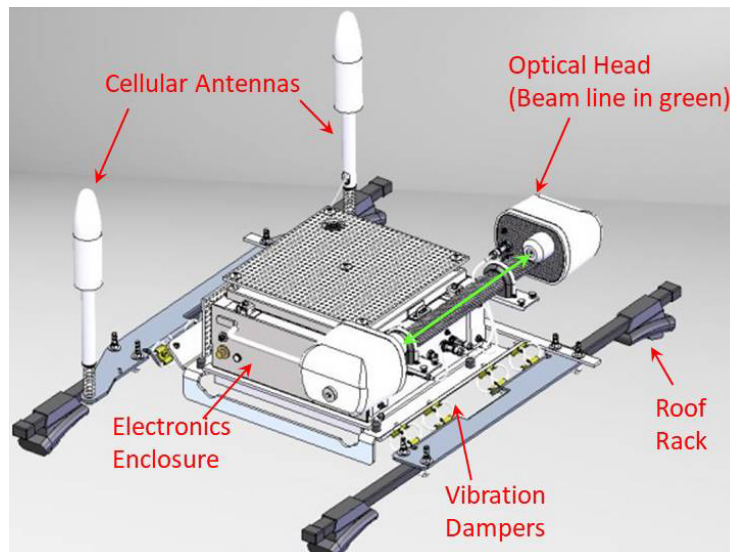


Fig. 3. Solid model of sensor as deployed on truck roof. Main components are labeled.

The electronics are housed in an IP-68 rated NEMA enclosure that has been designed for thermal performance and all-weather operation. In addition to the microprocessor and electronics, the enclosure also contains the laser source (and inline isolator and AOM), laser current and temperature controllers, PID temperature controllers for heating of the sensor head, pump line for mirror purge [30] and LTE cellular wireless gateway. The gateway is

used to relay aggregated sensor data to a computational cloud on a lossless store-and-forward basis. Large aperture cellular antennas are mounted outside the enclosure to ensure reliable connectivity in remote areas where low-band operation is prevalent. In addition, 2x2 MIMO is employed to further enhance link reliability and multi-carrier support is accommodated via dual radio architecture. The enclosure also includes a GPS sensor (Linx, RXM-GPS-FM-T) for timestamping and spatial localization, as well as sensors for external temperature (Omega, RTD-806) and pressure (Honeywell, PX2AM1XX001BAAAX) for calculation of concentration. The top of the enclosure includes a solar shield to prevent excessive conduction heating due to sunlight exposure. The electronics enclosure is designed to operate over -30 to $+50$ °C ambient and is limited primarily by the size of the laser Peltier element and thermal coefficient of expansion (CoE) of the mechanical structure. This proof-of-concept minimizes power consumption but, to minimize design complexity in this iteration, we have used a stock NEMA enclosure not yet optimized for size and weight. Future work will significantly reduce size and weight primarily through adoption of miniaturized electronics and a high level of integration.

The sensor head houses the optical cavity, along with the final steering mirrors and photo-detector. Light is coupled into the head via a fiber running from the enclosure box. A critical design aspect is to maintain cavity alignment and mirror reflectivity for field use where driving can induce significant vibration, temperature can change, precipitation can be present, and contaminants (dust, moisture, splash etc.) can be present in the air. The main structure of the cavity uses carbon-fiber to achieve low mass with relatively high rigidity and low thermal expansion. A single 2" diameter tube connects the two optical ends of the sensor to define the structure and provide a conduit for purge air and wire harness routing. Rounded, removable plastic caps enclose the head on either side. The head is thermally insulated and includes heaters to maintain uniform temperature for the optical cavity with <120 W of heating power. The heating circuit comprises two ceramic cartridge heaters that operate at <20 W each in each of the 2 caps along with a single tube heater at <40 W which surrounds the 2" tube; these are controlled by 3 PID temperature controllers (one for each cap, one for tube heater). Finally, to maintain cleanliness of the two HR mirrors, small purge flows are used to prevent ambient particles or splash from reaching the HR surfaces [30]. A single compact rotary-vane pump with inline particle and moisture filters pulls in air from the atmosphere (~ 3 slpm) and then passes that (filtered) air to small positive pressure regions near either HR mirror (see also Fig. 2). For (on-axis) CRDS the beam size within the cavity is only ~ 3 mm meaning that relatively low purge flows can be used (*cf.* multi-pass cells techniques with larger mirror diameters [22,40]). In some cases, we also shield the entire beam line with a perforated tube to further protect the mirrors without impacting the overall air flow through the open-cavity.

3. Laboratory testing

A series of tests were performed to confirm sensor accuracy and precision in the laboratory. For accuracy measurements, to deliver fixed and known concentrations, a closed-path setup was temporarily used (i.e. a pump and flow cell tube were installed). The gas delivery setup consisted of two gas cylinders each with a mass-flow controller. A mixture of 250 ppm methane with nitrogen balance (from one tank) was mixed with ultra-high purity grade nitrogen (from second tank) to set desired methane concentrations. Figure 4 shows the results of measured concentrations for a series of actual (delivered) concentrations. Each measurement was a 2 minute average of individual readings at 1 s intervals. Error bars on actual concentration are based on the uncertainties of the two mass-flow controllers, while error bars on measured concentration are found as the standard error. The two series of concentrations agree very well, within experimental uncertainty in all cases. Delivering known and fixed methane concentrations to the open-path sensor is experimentally challenging but our past work (with an open-path CRDS sensor using similar spectroscopy

but at 1742 nm) has shown consistent reading between our open-instrument and a reference commercial CRDS analyzer thereby supporting the accuracy of our open-path scheme [30].

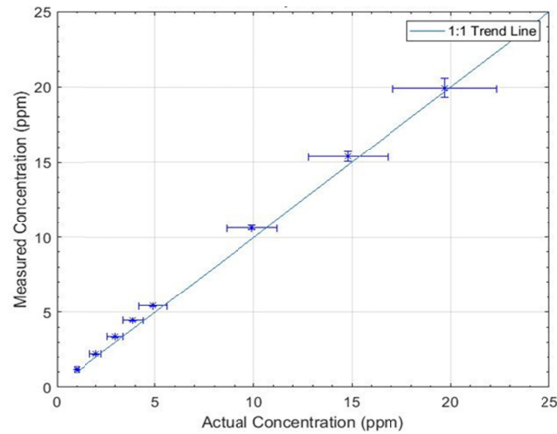


Fig. 4. Plot of measured versus actual methane concentration to examine sensor accuracy.

Sensitivity tests were performed for the open-path sensor through Allan Deviation studies [41,42] which provides a statistical method to look at measurement stability. Results of these tests for open-path operation at quasi-stable lab background (with 1-s measurement intervals) are shown in Fig. 5 and reveal an Allan variance of ~ 10 ppb/s at 1-second. Repeating such measurements yields results in the range of 10-15 ppb (referenced to 1 s) depending on particle loading in the lab air and exact sensor alignment conditions.

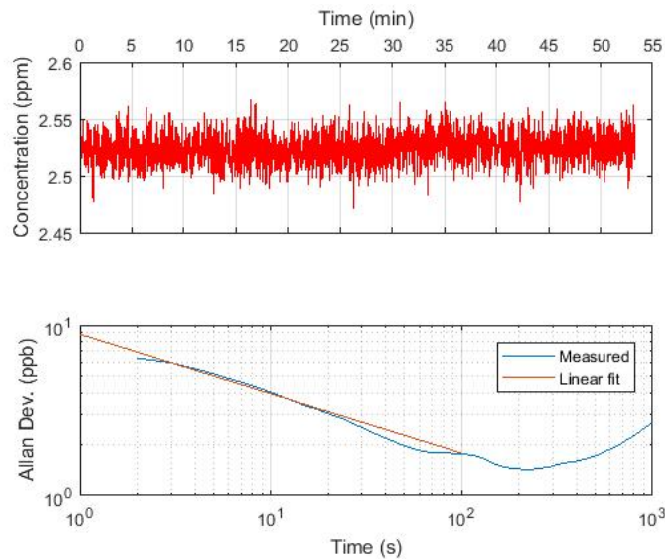


Fig. 5. Top: Time series of CH_4 concentrations. Bottom: Resulting Allan deviation as function of sampling time.

4. Field testing

We have extensively field tested the sensor in a series of driving campaigns in north eastern Colorado, southern Wyoming and the Marcellus Shale region of Pennsylvania [43]. The measurements were performed at different times of year in varied weather conditions (temperature, wind, and precipitation) as well as different road types (blacktop and potholed gravel etc.). Figure 6 shows an image of truck mounted sensor.



Fig. 6. Photograph of truck with roof-mounted methane sensor.

4.1. Sensor performance under varying field conditions

We have analyzed the field data to examine sensor performance under varying field conditions. We are particularly interested in the sensitivity of baseline CH_4 (based on the 1-second Allan Deviation) under different ambient conditions. For detection of elevated methane plumes one requires that they be discernible relative to the (\sim flat) baseline. To address this, we have extracted a series of data segments (30 s each) from the data. We only accept CH_4 data that pass certain Quality Control (QC) tests; in particular, we only maintain readings where the mirror reflectivity remains above $R = 0.9999$, as can be diagnosed from the baseline fit parameter, b , of Eq. (1). Other QC parameters include the number of ring-downs ingested per second, which we normally require to be >300 (but can very occasionally fall below the target, for example in cases where we drive immediately behind a vehicle emitting exhaust with large particle content), and the detector baseline level (voltage with no incident light) the variation of which is indicative of detector degradation. For looking at baseline stability, we reject segments containing elevated (plume) readings as these would bias the baseline statistics. We have examined slightly over 1 million raw (1 Hertz) CH_4 concentration readings from ~ 280 hours of drive data, from which we find $\sim 25,000$ usable baseline segments. The median (1-second) Allan deviation of these segments is 25 ppb (while the mean is 28 ppb). The first conclusion is there is slight degradation in sensitivity, by a factor of ~ 2 , for mobile (driving) measurements as compared to laboratory measurements. This is explained by several factors: collecting some data with slightly poorer R , more particle loading in the air, and collecting data at colder temperatures where alignment is affected (see below). Maintaining a sensitivity of better than 30 ppb under these diverse field conditions is a very positive result for practical plume detection (see below).

We have examined the data to consider the factors influencing the field sensitivity. We find that the vehicle speed (over ~ 0 -75 km/hr) has very minimal influence on sensitivity given that the median deviation is 25 ppb for all stationary readings as compared to 26 ppb for all moving readings, indicating that effects of vibration have been successfully dampened. As expected from preparatory cold-chamber tests, the measurement sensitivity has some dependence on ambient temperature (owing to thermal expansion of the cavity). Figure 7 shows a plot of the segment Allan deviations versus temperature (randomly plotting only 1/30th of the overall segments for visual clarity). The green line shows the median of all segment Allan deviations. Based on fitting these data (red curve), we find that the sensitivity

(Allan Deviation) holds within a factor of ~ 1.5 across the temperature range from -10 to 35 $^{\circ}\text{C}$. We fit with a parabolic instead of linear function as we expect a minimum at the alignment temperature of ~ 22 $^{\circ}\text{C}$. The temperature range is very adequate for many field applications and can be improved with modifications to the thermal system.

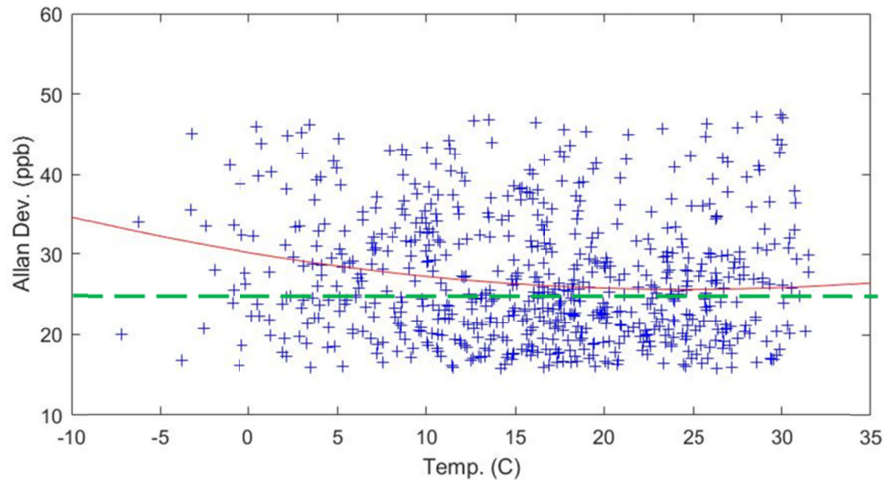


Fig. 7. Dependence of sensitivity (Allan Deviation) versus ambient temperature.

4.2. Plume detection examples

We have tested the ability of the sensor to detect methane plumes (i.e. elevated above background readings) from various sources including controlled releases as well as real natural gas infrastructure. The former tests were performed at the Methane Emissions Technology Evaluation Center (METEC) at Colorado State University. METEC is a purpose built facility where controlled releases of methane can be performed at conditions designed to be realistic of real oil and gas facilities [15]. Tests at METEC have spanned the range of emission rates that the facility can deliver, i.e. from ~ 0.03 g/s to ~ 1 g/s (at the time of our measurements). Figure 8 shows three examples of plumes detected by the truck-mounted sensor at the METEC facility at downwind locations. Readings are spaced by 1-s in all cases. The mass-flows and distance of the truck from the source are given in the figure. The readings were made at speeds of ~ 20 km/hr and the wind varied over ~ 2 - 4 m/s over the measurements. The plumes show the basic expected trends (e.g. wider and lower amplitude when further away, higher amplitude for higher mass flow) but individual plumes vary considerably (for given mass-flow and distance) due to wind and turbulent transport; for this reason, multiple plumes should be sampled to reliably infer source parameters [18–20].

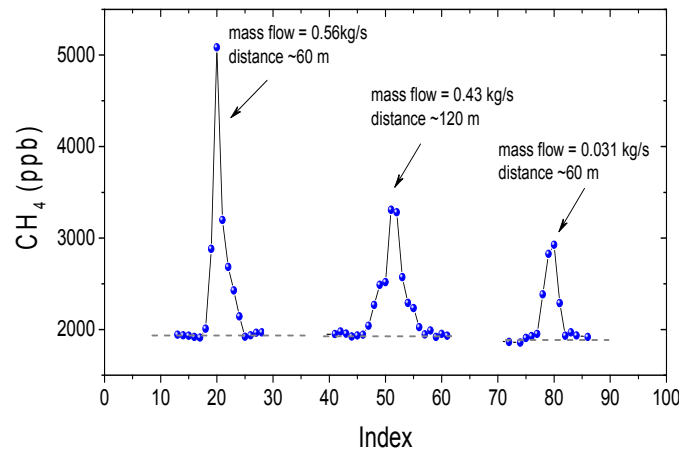


Fig. 8. Examples of plumes detected by the truck-mounted sensor at the METEC facility.

Figure 9 provides two brief examples of detection of elevated methane plumes as the sensor is driven past real oil and gas infrastructure. In both cases, one can see elevated plumes downwind of the oil and gas equipment (with baseline on either side). The top panel is due to a single pass with peak CH_4 concentration of 4.1 ppm. The lower panel is due to multiple back-and-forth passes by a larger site with distributed equipment over about 12 minutes (during which time the wind will also have some variation). Again, it is beyond the scope of this paper, but these types of concentration readings along with wind readings (from either a vehicle mounted or fixed weather station) can be used to locate and quantify methane emission sources [18–20]. In the Pennsylvania study, our collaborators also recorded VOC emissions that were found to correlate with the methane data [43].

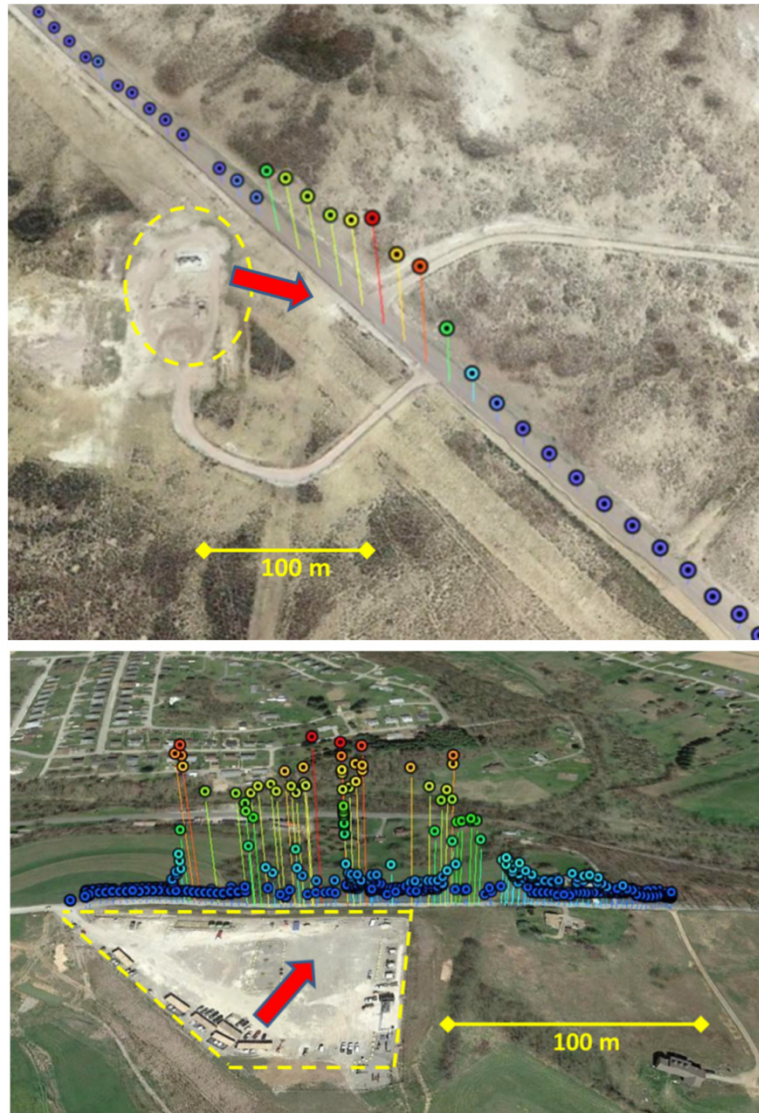


Fig. 9. Plume detection from real oil and gas equipment. Top: Single-pass along road in Wyoming/Colorado region. Bottom: Multiple passes along road in Pennsylvania. Broken yellow lines show perimeters containing oil and gas equipment; red arrows show wind direction. See text.

5. Conclusions

We have presented the design and testing of a purpose built open-path CRDS methane sensor for mobile sampling of natural gas emissions. The sensor is primarily designed for use on vehicles (e.g. trucks) but we have flown more compact version (without cellular and total mass including electronics and head of 7 kg) on a drone (Matrice 600 Pro) as will be published in the future. The open-path sensor yields sensitivity of 10-15 ppb in the lab and ~ 30 ppb for extended field use over a range of speeds, road conditions and temperatures (-10 to 35 °C; and these limits can be improved). The sensitivity is poorer than from commercial closed-path CRDS instruments (which are overly sensitive for this application), but is very adequate for practical emissions measurements. In addition to meeting the given

sensitivity target, the sensor also meets the temporal response and accuracy needs given in Section I with favorable SWAP including low power draw allowing direct connection to automobile batteries without other modifications. Future sensor versions may operate in the mid-infrared (MIR) where cross-sections are stronger, but the NIR telecom components are relatively low cost and maturely engineered.

Recent data [24] indicates that a sensitivity of ~ 100 ppb allows detection of mass flows as low as ~ 0.03 g/s within ~ 100 m of the source (and higher mass flows at larger distances), as we have shown with our instrument at the METEC facility. At the system level, detecting emissions of $> \sim 0.03$ g/s corresponds to measuring well over 95% of total emissions from real oil and gas fields based on published inventories and given the long-tail distribution of site emissions and super-emitters (e.g [19,44,45]).

The simplicity and autonomous nature of the sensors makes them well suited for mobile application including research purposes as well as commercial use on oil and gas company work trucks for monitoring of basins or enterprise regions. Such measurements would have the spatial granularity to monitor individual well sites and enable data-driven asset management (e.g. prioritization of repairs). The spatially resolved measurements can also complement coarser resolution satellite measurements [8–12].

Funding

Advanced Industries program from the Colorado Office of Economic Development and International Trade.

Acknowledgments

The authors gratefully acknowledge technical assistance from Simon Gassner, Darik Freeman, and Garrett Casassa (CZero).

References

1. Intergovernmental Panel on Climate Change (IPCC), “Climate Change 2014: Synthesis Report,” (Geneva, Switzerland, 2014).
2. S. Kirschke, P. Bousquet, P. Ciais, M. Saunois, J. G. Canadell, E. J. Dlugokencky, P. Bergamaschi, D. Bergmann, D. R. Blake, L. Bruhwiler, P. Cameron-Smith, S. Castaldi, F. Chevallier, L. Feng, A. Fraser, M. Heimann, E. L. Hodson, S. Houweling, B. Josse, P. J. Fraser, P. B. Krummel, J. F. Lamarque, R. L. Langenfelds, C. Le Quere, V. Naik, S. O’Doherty, P. I. Palmer, I. Pison, D. Plummer, B. Poulter, R. G. Prinn, M. Rigby, B. Ringeval, M. Santini, M. Schmidt, D. T. Shindell, I. J. Simpson, R. Spahni, L. P. Steele, S. A. Strode, K. Sudo, S. Szopa, G. R. van der Werf, A. Voulgarakis, M. van Weele, R. F. Weiss, J. E. Williams, and G. Zeng, “Three decades of global methane sources and sinks,” *Nat. Geosci.* **6**(10), 813–823 (2013).
3. Colorado Oil and Gas Conservation Committee, “COGCC GIS Online,” https://cogccmap.state.co.us/cogcc_gis_online, accessed May 7, 2019.
4. R. A. Alvarez, D. Zavala-Araiza, D. R. Lyon, D. T. Allen, Z. R. Barkley, A. R. Brandt, K. J. Davis, S. C. Herndon, D. J. Jacob, A. Karion, E. A. Kort, B. K. Lamb, T. Lauvaux, J. D. Maasackers, A. J. Marchese, M. Omara, S. W. Pacala, J. Peischl, A. L. Robinson, P. B. Shepson, C. Sweeney, A. Townsend-Small, S. C. Wofsy, and S. P. Hamburg, “Assessment of methane emissions from the U.S. oil and gas supply chain,” *Science* **361**(6398), 186–188 (2018).
5. A. Karion, C. Sweeney, G. Petron, G. Frost, R. M. Hardesty, J. Kofler, B. R. Miller, T. Newberger, S. Wolter, R. Banta, A. Brewer, E. Dlugokencky, P. Lang, S. A. Montzka, R. Schnell, P. Tans, M. Trainer, R. Zamora, and S. Conley, “Methane emissions estimate from airborne measurements over a western United States natural gas field,” *Geophys. Res. Lett.* **40**(16), 4393–4397 (2013).
6. S. Baray, A. Darlington, M. Gordon, K. L. Hayden, A. Leithead, S. M. Li, P. S. K. Liu, R. L. Mittermeier, S. G. Moussa, J. O’Brien, R. Staebler, M. Wolde, D. Worthy, and R. McLaren, “Quantification of methane sources in the Athabasca Oil Sands Region of Alberta by aircraft mass balance,” *Atmos. Chem. Phys.* **18**, 7361–7378 (2018).
7. J. Peischl, A. Karion, C. Sweeney, E. A. Kort, M. L. Smith, A. R. Brandt, T. Yeskoo, K. C. Aikin, S. A. Conley, A. Gvakharia, M. Trainer, S. Wolter, and T. B. Ryerson, “Quantifying atmospheric methane emissions from oil and natural gas production in the Bakken shale region of North Dakota,” *J. Geophys. Res. Atmos.* **121**(10), 6101–6111 (2016).
8. E. D. Fund, “This Space Technology Can Cut Climate Pollution on Earth,” <https://www.edf.org/climate/space-technology-can-cut-climate-pollution-earth>, accessed May 2, 2019.

9. GHGSat, “GHGSat-C1/C2,” <https://www.ghgsat.com/who-we-are/our-satellites/satellite-2/>, accessed May 2, 2019.
10. J. X. Sheng, D. J. Jacob, A. J. Turner, J. D. Maasackers, J. Benmergui, A. A. Bloom, C. Arndt, R. Gautam, D. Zavala-Araiza, H. Boesch, and R. J. Parker, “2010–2016 methane trends over Canada, the United States, and Mexico observed by the GOSAT satellite: contributions from different source sectors,” *Atmos. Chem. Phys.* **18**(16), 12257–12267 (2018).
11. D. H. Cusworth, D. J. Jacob, J. X. Sheng, J. Benmergui, A. J. Turner, J. Brandman, L. White, and C. A. Randles, “Detecting high-emitting methane sources in oil/gas fields using satellite observations,” *Atmos. Chem. Phys.* **18**(23), 16885–16896 (2018).
12. D. J. Jacob, A. J. Turner, J. D. Maasackers, J. X. Sheng, K. Sun, X. Liu, K. Chance, I. Aben, J. McKeever, and C. Frankenberg, “Satellite observations of atmospheric methane and their value for quantifying methane emissions,” *Atmos. Chem. Phys.* **16**(22), 14371–14396 (2016).
13. T. L. Vaughn, C. S. Bell, C. K. Pickering, S. Schwietzke, G. A. Heath, G. Pétron, D. J. Zimmerle, R. C. Schnell, and D. Nummedal, “Temporal variability largely explains top-down/bottom-up difference in methane emission estimates from a natural gas production region,” *Proc. Natl. Acad. Sci. U.S.A.* **115**(46), 11712–11717 (2018).
14. M. R. Johnson, D. R. Tynner, S. Conley, S. Schwietzke, and D. Zavala-Araiza, “Comparisons of Airborne Measurements and Inventory Estimates of Methane Emissions in the Alberta Upstream Oil and Gas Sector,” *Environ. Sci. Technol.* **51**(21), 13008–13017 (2017).
15. A. P. Ravikumar, J. Wang, M. McGuire, C. S. Bell, D. Zimmerle, and A. R. Brandt, ““Good versus Good Enough?” Empirical Tests of Methane Leak Detection Sensitivity of a Commercial Infrared Camera,” *Environ. Sci. Technol.* **52**(4), 2368–2374 (2018).
16. Heath, “Optical Methane Detector,” <https://heathus.com/products/optical-methane-detector-omd/>, accessed June 21, 2019.
17. Heath, “Remote Methane Leak Detector,” <https://heathus.com/products/remote-methane-leak-detector/>, accessed June 21, 2019.
18. J. D. Albertson, T. Harvey, G. Foderaro, P. Zhu, X. Zhou, S. Ferrari, M. S. Amin, M. Modrak, H. Brantley, and E. D. Thoma, “A Mobile Sensing Approach for Regional Surveillance of Fugitive Methane Emissions in Oil and Gas Production,” *Environ. Sci. Technol.* **50**(5), 2487–2497 (2016).
19. H. L. Brantley, E. D. Thoma, W. C. Squier, B. B. Guven, and D. Lyon, “Assessment of Methane Emissions from Oil and Gas Production Pads using Mobile Measurements,” *Environ. Sci. Technol.* **48**(24), 14508–14515 (2014).
20. D. R. Caulton, Q. Li, E. Bou-Zeid, J. P. Fitts, L. M. Golston, D. Pan, J. Lu, H. M. Lane, B. Buchholz, X. H. Guo, J. McSpirt, L. Wendt, and M. A. Zondlo, “Quantifying uncertainties from mobile-laboratory-derived emissions of well pads using inverse Gaussian methods,” *Atmos. Chem. Phys.* **18**(20), 15145–15168 (2018).
21. L. M. Golston, N. F. Aubut, M. B. Frish, S. T. Yang, R. W. Talbot, C. Gretencord, J. McSpirt, and M. A. Zondlo, “Natural Gas Fugitive Leak Detection Using an Unmanned Aerial Vehicle: Localization and Quantification of Emission Rate,” *Atmosphere* **9**(9), 333 (2018).
22. A. Khan, D. Schaefer, L. Tao, D. J. Miller, K. Sun, M. A. Zondlo, W. A. Harrison, B. Roscoe, and D. J. Lary, “Low Power Greenhouse Gas Sensors for Unmanned Aerial Vehicles,” *Remote Sens.* **4**(5), 1355–1368 (2012).
23. C. S. Bell, T. L. Vaughn, D. Zimmerle, S. C. Herndon, T. I. Yacovitch, G. A. Heath, G. Petron, R. Edie, R. A. Field, S. M. Murphy, A. M. Robertson, and J. Soltis, “Comparison of methane emission estimates from multiple measurement techniques at natural gas production pads,” *Elementa-Sci. Anthropocene* **5**, 14 (2017).
24. E. Thoma, H. Brantley, and J. D. Albertson, “Fugitive methane assessment with mobile and fence line sensors,” in *CH4 Connections Workshop* (GTI, 2014).
25. A. Arfire, A. Marjovi, and A. Martinoli, “Mitigating Slow Dynamics of Low-Cost Chemical Sensors for Mobile Air Quality Monitoring Sensor Networks,” in *Proceedings of the 2016 International Conference on Embedded Wireless Systems and Networks*, (Junction Publishing, 2016), pp. 159–167.
26. J. K. Lee, A. Christen, R. Ketler, and Z. Nestic, “A mobile sensor network to map carbon dioxide emissions in urban environments,” *Atmos. Meas. Tech.* **10**(2), 645–665 (2017).
27. J. S. Apte, K. P. Messier, S. Gani, M. Brauer, T. W. Kirchstetter, M. M. Lunden, J. D. Marshall, C. J. Portier, R. C. H. Vermeulen, and S. P. Hamburg, “High-Resolution Air Pollution Mapping with Google Street View Cars: Exploiting Big Data,” *Environ. Sci. Technol.* **51**(12), 6999–7008 (2017).
28. G. Berden, R. Peeters, and G. Meijer, “Cavity ring-down spectroscopy: Experimental schemes and applications,” *Int. Rev. Phys. Chem.* **19**(4), 565–607 (2000).
29. B. A. Paldus and A. A. Kachanov, “An historical overview of cavity enhanced methods,” *Can. J. Phys.* **83**(10), 975–999 (2005).
30. L. E. McHale, A. Hecobian, and A. P. Yalin, “Open-path cavity ring-down spectroscopy for trace gas measurements in ambient air,” *Opt. Express* **24**(5), 5523–5535 (2016).
31. Picarro, “PICARRO G2301 CRDS Analyzer CO2 CH4 H2O Measurements in Air,” http://www.picarro.com/products_solutions/trace_gas_analyzers/co_co2_ch4_h2o, accessed March 4, 2017.
32. C. L. Hagen, B. C. Lee, I. S. Franka, J. L. Rath, T. C. VandenBoer, J. M. Roberts, S. S. Brown, and A. P. Yalin, “Cavity ring-down spectroscopy sensor for detection of hydrogen chloride,” *Atmos. Meas. Tech.* **7**(2), 345–357 (2014).
33. S. S. Brown, “Absorption spectroscopy in high-finesse cavities for atmospheric studies,” *Chem. Rev.* **103**(12), 5219–5238 (2003).

34. J. C. von Fischer, D. Cooley, S. Chamberlain, A. Gaylord, C. J. Griebenow, S. P. Hamburg, J. Salo, R. Schumacher, D. Theobald, and J. Ham, "Rapid, Vehicle-Based Identification of Location and Magnitude of Urban Natural Gas Pipeline Leaks," *Environ. Sci. Technol.* **51**(7), 4091–4099 (2017).
35. Z. D. Weller, D. K. Yang, and J. C. von Fischer, "An open source algorithm to detect natural gas leaks from mobile methane survey data," *PLoS One* **14**(2), e0212287 (2019).
36. A. Pettersson, E. R. Lovejoy, C. A. Brock, S. S. Brown, and A. R. Ravishankara, "Measurement of aerosol optical extinction at 532nm with pulsed cavity ring down spectroscopy," *J. Aerosol Sci.* **35**(8), 995–1011 (2004).
37. L. S. Rothman, I. E. Gordon, A. Barbe, D. Chris Benner, P. F. Bernath, M. Birk, V. Boudon, A. C. L. R. Brown, J.-P. Champion, K. Chance, L. H. Coudert, V. Dana, V. M. Devi, S. Fally, J.-M. Flaud, R. R. Gamache, A. Goldman, D. Jacquemart, I. Kleiner, N. Lacombe, W. J. Lafferty, J.-Y. Mandin, S. T. Massie, S. N. Mikhailenco, C. E. Miller, O. V. N. N. Moazzen-Ahmadi, A. V. Nikitin, J. Orphal, V. I. Perevalov, A. Perrin, A. Predoi-Cross, C. P. Rinsland, M. Rotger, M. Šimečková, M. A. H. Smith, S. A. T. K. Sung, J. Tennyson, R. A. Toth, A. C. Vandaele, and J. Vander Auwera, "The HITRAN 2008 Molecular Spectroscopic Database," *J. Quant. Spectrosc. Radiat. Transf.* **110**(9-10), 533–572 (2009).
38. H. Kogelnik and T. Li, "Laser beams and resonators," *Appl. Opt.* **5**, 1550 (1966).
39. J. B. Dudek, P. B. Tarsa, A. Velasquez, M. Wladyslawski, P. Rabinowitz, and K. K. Lehmann, "Trace moisture detection using continuous-wave cavity ring-down spectroscopy," *Anal. Chem.* **75**(17), 4599–4605 (2003).
40. D. S. Baer, J. B. Paul, M. Gupta, and A. O'Keefe, "Sensitive absorption measurements in the near infrared region using off-axis integrated-cavity output spectroscopy," *Appl. Phys. B* **75**(2-3), 261–265 (2002).
41. P. Werle, R. Mucke, and F. Slemr, "The limits of signal averaging in atmospheric trace-gas monitoring by tunable diode-laser absorption-spectroscopy (TDLAS)," *Appl. Phys., B Photophys. Laser Chem.* **57**, 131–139 (1993).
42. H. Huang and K. K. Lehmann, "Sensitivity Limits of Continuous Wave Cavity Ring-Down Spectroscopy," *J. Phys. Chem. A* **117**(50), 13399–13411 (2013).
43. X. Zhou, A. Montazeri, L. McHale, S. Gassner, D. Lyon, B. Trask, J. Gu, A. P. Yalin, and J. D. Albertson, "Characterization of methane and volatile organic compounds (VOCs) emissions from natural gas production sites: a mobile sensing approach," in *American Geophysical Union*, New Orleans, LA, 2017.
44. D. R. Lyon, D. Zavala-Araiza, R. A. Alvarez, R. Harriss, V. Palacios, X. Lan, R. Talbot, T. Lavoie, P. Shepson, T. I. Yacovitch, S. C. Herndon, A. J. Marchese, D. Zimmerle, A. L. Robinson, and S. P. Hamburg, "Constructing a Spatially Resolved Methane Emission Inventory for the Barnett Shale Region," *Environ. Sci. Technol.* **49**(13), 8147–8157 (2015).
45. D. Zavala-Araiza, D. Lyon, R. A. Alvarez, V. Palacios, R. Harriss, X. Lan, R. Talbot, and S. P. Hamburg, "Toward a Functional Definition of Methane Super-Emitters: Application to Natural Gas Production Sites," *Environ. Sci. Technol.* **49**(13), 8167–8174 (2015).